



**HAL**  
open science

# Riemannian Clustering of PolSAR Data using the Polar Decomposition

Madalina Ciuca, Gabriel Vasile, Marco Congedo, Michel Gay

► **To cite this version:**

Madalina Ciuca, Gabriel Vasile, Marco Congedo, Michel Gay. Riemannian Clustering of PolSAR Data using the Polar Decomposition. C.H. Chen. Signal and Image Processing for Remote Sensing, 3rd edition, CRC Press, 2024, Signal and Image Processing of Earth Observations, ISBN 9781032437415. hal-03839678v3

**HAL Id: hal-03839678**

**<https://hal.science/hal-03839678v3>**

Submitted on 10 Nov 2023

**HAL** is a multi-disciplinary open access archive for the deposit and dissemination of scientific research documents, whether they are published or not. The documents may come from teaching and research institutions in France or abroad, or from public or private research centers.

L'archive ouverte pluridisciplinaire **HAL**, est destinée au dépôt et à la diffusion de documents scientifiques de niveau recherche, publiés ou non, émanant des établissements d'enseignement et de recherche français ou étrangers, des laboratoires publics ou privés.

Copyright

*Madalina Ciuca, Gabriel Vasile, Marco Congedo, Michel Gay*

---

# ***Riemannian Clustering of PolSAR Data using the Polar Decomposition***

# Chapter 1

---

## *Riemannian Clustering of PolSAR Data using the Polar Decomposition*

1.1	Introduction .....	1
1.1.1	PolSAR clustering .....	2
1.1.2	Distance metrics for PolSAR data .....	3
1.1.3	Chapter contribution .....	3
1.2	From coherent polar decomposition to classification on a Riemannian manifold .....	4
1.2.1	The polar decomposition .....	4
1.2.2	Riemannian manifold and corresponding distances .....	6
1.2.3	Unitary manifold and corresponding distances .....	7
1.2.4	Hermitian matrices and Riemannian geometry in PolSAR .....	8
1.2.5	Manifold Gradient with Sobel Kernel .....	9
1.2.6	Proposed method .....	10
1.3	Results and discussion .....	11
1.3.1	Simulated datasets .....	12
1.3.1.1	Simulated data with different intensities and covariance matrices .....	12
1.3.1.2	Simulated monostatic backscattering response of a dihedral .....	13
1.3.2	Real datasets .....	16
1.3.2.1	Hermitian barycenters gradient and unitary barycenters parameter estimation .....	16
1.3.2.2	Clustering results .....	19
1.4	General Remarks and Conclusions .....	22
1.5	Glossary .....	24

“nobreak

## 1.1 Introduction

Polarimetric Synthetic Aperture Radar (PolSAR) data records the scattering diversity by measuring the electromagnetic response in two orthogonal polarization bases. The target decomposition algorithms are generally employed in the polarimetric signature analysis. They can be either coherent or incoherent. The distinction depends on whether the scattering or the covariance<sup>1</sup> matrices are used, respectively. While the first is a directly measured quantity for a full-polarimetric PolSAR pixel, the latter is a second-order statistical estimate.

One important application in PolSAR data analysis is classification. While both supervised and unsupervised methods are popular and have various levels of accuracy, this article will focus only on the case of unsupervised classification. Particularly, clustering techniques are discussed.

### 1.1.1 PolSAR clustering

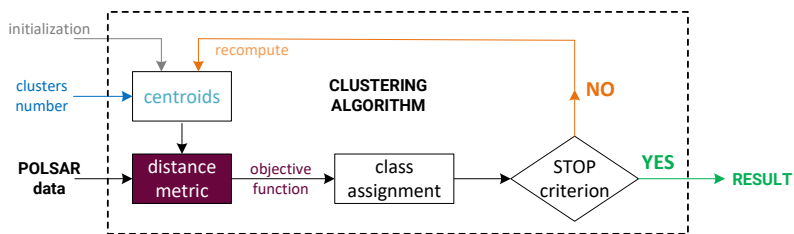


FIGURE 1.1: Generic scheme of a centroid-based clustering algorithm for PolSAR data.

In computer science, clustering methods are divided into several groups, as for example: partitional, hierarchical, density, grid or model-based [1]. While such methods are popular for PolSAR unsupervised classification, centroid-based approaches belonging to the partitional category are the most prevalent. A generic scheme of a centroid-based clustering algorithm is presented in Fig. 1.1.

The introduction of the Wishart classifier has been a major milestone in PolSAR unsupervised classification [31, 33]. It was shown to represent an optimal Bayesian classifier, considering that the scattering vectors are modeled by zero mean complex circular Gaussian vectors, completely characterized by

<sup>1</sup>also coherency. In the current text, mentioning one automatically implies the other, as they have similar statistical properties.



their covariance matrix [31]. It uses a metric known as the Wishart similarity measure. The initialization of the centroids is obtained by the  $H - \alpha$  decomposition [15]. This is applied as a prerequisite and an estimate centroid is provided for each class in the  $H - \alpha$  plane (which fixes the number of clusters to eight). After each run, the centroids are updated by averaging the redistributed matrices of each class.

With the constant increase in spatial resolution, different non-Gaussian clustering strategies have been adopted for PolSAR data classification. Based on the conventional product model, we can distinguish two main directions in introducing heterogeneity. By adopting either non-Gaussian target vectors (such as K-, Kummer-U,  $G_0$ -distributed clutter models) or compound covariance/coherencies (like scale mixtures,  $G_0$ - or K-Wishart models) different classification algorithms have been proposed [57, 18, 7, 20, 19, 28].

Being simple and effective, the Wishart classification still remains one of the most employed clustering methods in practical applications. Its popularity and fundamental importance has been proven also by many publications, which by modifying one or more stages in the generic schema (Fig. 1.1) have arrived to new or improved versions. Notable changes can be found in the: a) initialization and number of clusters [10, 34, 43], b) class assignment logic [34], or c) the distance metric. Nonetheless, the latter deserves a discussion on its own.

### 1.1.2 Distance metrics for PolSAR data

Depending on the optimization strategy, the two main groups of PolSAR distances are stochastic and geometric. The Wishart similarity measure is probably the most used stochastic similarity/dissimilarity measure with both unsupervised and supervised methods. As the statistics of the scattering vector/covariance matrices have been improved, the distance metrics used in classification (or filtering) algorithms have also evolved. Non-exhaustive examples of such metrics are the revised-Wishart, the Bartlett, the Hellinger, the Kullback-Leibler, the Bhattacharyya, the Rényi or the Chi-square, either with a local [25] or a non-local approach [27].

Geometric metrics are optimized with respect to a specific geometric space and usually allow the computation on the principle of the shortest path. Some examples are the Euclidean, the Riemannian affine invariant (introduced in Section 1.2), the log-Euclidean, or the angular geodesic [43] distances.

A concise indexing of similarity/dissimilarity measures used in PolSAR is available in [55], while a more in-depth review can be found in [42].

### 1.1.3 Chapter contribution

This chapter presents a new framework for geometrical k-means PolSAR clustering based on two important aspects: 1) the polar decomposition mathematical properties and 2) the Riemannian geometry. This framework is no

#### 4 Riemannian Clustering of PolSAR Data using the Polar Decomposition

longer based on the use of covariance/coherency matrices. Instead, we directly exploit the scattering matrix by applying the polar decomposition. We study the properties of the two decomposition factors and conclude that only the Hermitian factor can serve as a rotation-invariant input for the clustering method.

No data vectorization is performed (compared to the case of constructing the scattering vectors) and the algorithm is designed to exploit the geometrical embedding of the Hermitian factors, which are inherently located on a Riemannian manifold. Instead of statistically averaging the scattering vectors (as for covariance/coherency matrix estimation), a local mean (i.e., barycenter) is computed based on a geodesic distance associated to the manifold. In other words, the algorithm does not modify, but takes advantage of both the algebraic and the geometric structure of its input features. No underlying statistical (homogeneous or heterogeneous) clutter model is therefore assumed.

Both simulated and real full-polarimetric PolSAR data are employed for validation. The proposed method is tested against the results obtained using the classical k-means framework with two alternative distance metrics: one stochastic – the Wishart similarity measure and one geometric – angular geodesic. With real data, we observe it recovers the texture information and some of the details lost in the second order statistical approach.

The remainder of this chapter is organized as follows. Section 1.2 offers some background on the use of the polar decomposition. It then focuses on defining concepts and tools necessary for applying the Riemannian manifolds theory with PolSAR data. Finally, it introduces the description of the proposed method. Section 1.3 analyses the experimental results. The conclusion and perspectives for future work are discussed in Section 1.4.

---

## 1.2 From coherent polar decomposition to classification on a Riemannian manifold

This section establishes the link between the polarimetric polar decomposition and metric based classification schemes on a Riemannian manifold.

### 1.2.1 The polar decomposition

Any complex square matrix  $\mathbf{S} \in \mathbb{C}^{n \times n}$  can be decomposed using the polar decomposition as the product of two factors: a *unitary matrix* ( $\mathbf{U}$ ,  $\mathbf{U}\mathbf{U}^H = \mathbf{I}$ ,  $\mathbf{U} \in \mathbb{C}^{n \times n}$ ) and a *Hermitian matrix* ( $\mathbf{H}$ ,  $\mathbf{H}^H = \mathbf{H}$ ,  $\mathbf{H} \in \mathbb{C}^{n \times n}$ ).  $\mathbf{H}$  is positive semi-definite (PSD), thus  $\mathbf{v}^H \mathbf{H} \mathbf{v} \geq 0$  for any nonzero column with complex

elements vector<sup>1</sup>,  $\mathbf{v} \in \mathbb{C}$ . In any unitarily invariant norm,  $\mathbf{U}$  is the nearest unitary matrix to  $\mathbf{S}$  [38]. The influence of the two factors is interpreted as follows: the unitary factor performs a rotation, while the Hermitian factor acts as a stretching/deformation.

There exist two different forms of this factorization, with (1.1) being known as the left polar decomposition and (1.2) as the right polar decomposition:

$$\mathbf{S} = \mathbf{U}\mathbf{H} \quad (1.1) \quad \mathbf{S} = \mathbf{K}\mathbf{U}. \quad (1.2)$$

The left/right Hermitian factors are obtained as:  $\mathbf{H} = (\mathbf{S}^H\mathbf{S})^{1/2}$  and  $\mathbf{K} = (\mathbf{S}\mathbf{S}^H)^{1/2}$ . If  $\mathbf{S}$  is a normal matrix (i.e., it verifies  $\mathbf{S}^H\mathbf{S} = \mathbf{S}\mathbf{S}^H$ ), it immediately follows that  $\mathbf{H} = \mathbf{K}$ . For all other  $\mathbf{S}$  matrices,  $\mathbf{S}^H\mathbf{S}$  is similar to  $\mathbf{S}\mathbf{S}^H$ . This means that  $\mathbf{H}$  and  $\mathbf{K}$  are themselves similar (i.e., have the same eigenvalues and the same number of independent eigenvectors). By using the properties of the unitary  $\mathbf{U}$  factor, (1.1) can be written using a mathematical artifice, as:  $\mathbf{S} = \mathbf{U}\mathbf{H}\mathbf{U}^H\mathbf{U} = (\mathbf{U}\mathbf{H}\mathbf{U}^H)\mathbf{U} = \mathbf{K}\mathbf{U}$ . As a result,  $\mathbf{K} = \mathbf{U}\mathbf{H}\mathbf{U}^H = \mathbf{U}\mathbf{H}\mathbf{U}^{-1}$ , which is the similarity equivalence.

From a mathematical perspective, the polar decomposition has a close connection to the Singular Value Decomposition (SVD), from which it can be computed. As a direct consequence, this decomposition can be inherently applied to any complex matrix. While the Hermitian factor ( $\mathbf{H}$  or  $\mathbf{K}$ ) from the decomposition is always unique, the unitary term is unique only if matrix  $\mathbf{S}$  is non-singular.

In PolSAR, the polar decomposition has been generally used as a coherent technique allowing feature extraction from the scattering matrix,  $\mathbf{S} \in \mathbb{C}^{2 \times 2}$ . Since there are no constraints in applying the factorization, it can be used for both symmetric/asymmetric, or otherwise, monostatic/bistatic scattering matrices.

The pioneering works of Carrea et al. [11, 12] have initially described the behavior of the two decomposition factors. The Hermitian positive semi-definite matrix is referred as a "boost" matrix.

Otherwise, references [49, 50, 51] express the scattering matrix polar decomposition using the formalism of quaternions and derive descriptive features from the polar factors. They propose both a coherent approach on single-look (also, 1-look) quad-pol data, as well as a generalization for incoherent multi-look data.

In optical polarimetry, the polar decomposition splits a complex  $2 \times 2$  Jones matrix in a retarder (i.e., the unitary matrix) and a diattenuator (i.e., the Hermitian matrix). The same significance is attributed to the two products obtained from decomposing a nondepolarizing Mueller matrix [35], while

---

<sup>1</sup>Notation: Boldface is used for vectors and matrices, with the first using lowercase and the second upper-case letters.

$\mathbf{I}$  denotes the identity matrix of size  $n \times n$ . Known operators are:  $(\cdot)^T$  as the transpose,  $(\cdot)^*$  as the complex conjugate, and  $(\cdot)^H$  as the conjugate-transpose.  $\|\cdot\|_F$  refers to the Frobenius norm, while  $|\cdot|$  is the absolute value.

a generalized polar decomposition (retarder, diattenuator and depolarizer factors extraction) is further proposed for a general Mueller matrix. Classification is performed coherently (i.e., in a pixel-by-pixel manner) in [54], on real PolSAR data in Mueller matrix format, following the above-mentioned generalized polar decomposition model.

In the proposed method, the polar decomposition is used to decompose the scattering matrix, but clustering technique applies only to the Hermitian terms. More details of the algorithm implementation are given in Subsection 1.2.6.

### 1.2.2 Riemannian manifold and corresponding distances

It is well known that positive-definite matrices are naturally embedded in a non-linear, smooth differentiable manifold. On such a manifold, the shortest path connecting any two points is named a geodesic: it is not a straight line, as in the Euclidean space, but a path which follows the curvature of the space.

Applying a suitable metric on the tangent bundle yields a Riemannian manifold,  $\mathbb{P}(n)$ . The best-known metric used for the PSD manifold is the affine invariant Riemannian metric (AIRM) [16].

For any two positive definite matrices  $\mathbf{A}$  and  $\mathbf{B}$ , AIRM provides a closed-form distance measure

$$d_{geod, \mathbb{P}(n)}(\mathbf{A}, \mathbf{B}) = \|\log(\mathbf{A}^{-1/2}\mathbf{B}\mathbf{A}^{-1/2})\|_F, \quad (1.3)$$

which can be interpreted as a similarity/dissimilarity criterion. Operator  $\log(\mathbf{X})$  represents the matrix logarithm. For positive-definite matrices it is usually computed using the eigenvalue decomposition:  $\mathbf{X} = \mathbf{V}\mathbf{D}\mathbf{V}^H$ ,  $\mathbf{D} = \text{diag}(\lambda_1, \lambda_2, \dots, \lambda_n)$  and the usual logarithm function. The operator  $\text{diag}(\cdot)$  returns a diagonal matrix having the elements inside parenthesis on the main diagonal. Then,  $\mathbf{D}_{log} = \text{diag}(\log(\lambda_1), \log(\lambda_2), \dots, \log(\lambda_n))$  and

$$\log(\mathbf{X}) = \mathbf{V} \cdot \mathbf{D}_{log} \cdot \mathbf{V}^H. \quad (1.4)$$

The AIRM geodesic distance complies to several invariance properties such as self-duality, congruence invariance, joint homogeneity and determinant identity, among others [16]. In particular, the congruence (or, affine) invariance reads

$$d_{geod, \mathbb{P}(n)}(\mathbf{J}\mathbf{A}\mathbf{J}^H, \mathbf{J}\mathbf{B}\mathbf{J}^H) = d_{geod, \mathbb{P}(n)}(\mathbf{A}, \mathbf{B}), \quad (1.5)$$

for any non-singular matrix  $\mathbf{J}$ .

For real PolSAR data, due the presence of noise (thermal or speckle), the Hermitian factors of the observed scattering matrices are always positive definite. They lie on a PSD Riemannian manifold with dimension  $n = 3$ . We can associate to any general matrix  $\mathbf{H}$ ,

$$\mathbf{H} = \begin{pmatrix} h_{11} & h_{12} \\ h_{12}^* & h_{22} \end{pmatrix}, \quad (1.6)$$

a point in  $\mathbb{R}^3$ , according to the mapping [37]:

$$\mathcal{F}(\mathbf{H}) = \frac{1}{\sqrt{2}} [h_{12} + h_{12}^*, h_{22} - h_{11}, h_{22} + h_{11}]. \quad (1.7)$$

For  $m$  positive definite matrices  $\{\mathbf{H}_1, \mathbf{H}_2, \dots, \mathbf{H}_m\}$ ,  $m > 2$ , the Riemannian barycenter, i.e., geometric center of mass or geometric mean, is a point  $\mathbf{H}_0$  which attains the minimum value of [6]

$$\arg \min_{\mathbf{H}_0} \sum_{i=1}^m d_{geod, \mathbb{P}(n)}(\mathbf{H}_0, \mathbf{H}_i)^2. \quad (1.8)$$

It is worth mentioning that the Riemannian mean presents some invariant properties. Among others [37]:

- permutation invariance:  
 $\mathbf{H}_0$  is still the solution considering any rearrangement of the original set  $\{\mathbf{H}_i\}$ ,  $1 \leq i \leq m$ .
- congruence invariance:  
 Changing the matrix set to  $\{\mathbf{V}\mathbf{H}_i\mathbf{V}^H\}$ ,  $1 \leq i \leq m$ ,  $\mathbf{V}$  non-singular, the barycenter changes accordingly, becoming  $\mathbf{V}\mathbf{H}_0\mathbf{V}^H$ .
- inversion invariance:  
 $\mathbf{H}_0^{-1}$  is the corresponding barycenter for the set of inverse matrices  $\{\mathbf{H}_i^{-1}\}$ ,  $1 \leq i \leq m$ .

It was shown that, on the Riemannian manifolds of positive-definite matrices, the solution to the minimization problem in (1.8) always exists and is unique [21, 5]. While there is no closed-form solution, convergent results are obtained by iterative minimization methods, for example based on a gradient descent [37, 5].

### 1.2.3 Unitary manifold and corresponding distances

On the manifold of unitary matrices,  $\mathbb{U}(n)$ , the geodesic distance between two generic matrices  $\mathbf{A}$  and  $\mathbf{B}$  is [21]:

$$d_U(\mathbf{A}, \mathbf{B}) = \|\log(\mathbf{A}^H \mathbf{B})\|_F. \quad (1.9)$$

The space of unitary matrices is a Lie group, endorsed with a Lie algebra. Computing the barycenter of  $p$  unitary matrices  $\{\mathbf{U}_1, \mathbf{U}_2, \dots, \mathbf{U}_p\}$  is addressed often in relation to the properties of this Lie space. The barycenters are computed using a distance-minimization method, similar to the Hermitian case by (1.8). Sometimes a projective iteration algorithm (i.e., based on projections to the Lie algebra and back into the Lie group) is used for the task [21]. To the best of our knowledge, there is no closed-form solution neither for this computation.

The update rule for calculating the average of matrices  $\{\mathbf{U}_j\}$ ,  $1 \leq j \leq p$  used in the current experiments is:

$$\mathbf{U}_{\mathbf{k}+1} = \mathbf{U}_{\mathbf{k}} \cdot \exp \left[ \frac{1}{N} \sum_{j=1} \log(\mathbf{U}_{\mathbf{k}}^H \mathbf{U}_j) \right]. \quad (1.10)$$

Operator  $\exp(\cdot)$  represents the matrix exponential and is the inverse operation of  $\log(\cdot)$ . These two operations no longer have a simplified form with unitary matrices. Moreover, for computing the barycenter in the manifold of unitary matrices, a simple gradient descent may not always converge due to numerical problems.

This work focuses particularly on the Hermitian factors, only computing some barycenter of unitary factors for illustration purposes. Therefore, while more sophisticated solutions may exist, they are not addressed here.

Given the interpretation of a unitary matrix as a complex rotation matrix (normal rotation and phase terms), we argue there is a significant advantage in eliminating this rotation from the original PolSAR scattering matrix.

#### 1.2.4 Hermitian matrices and Riemannian geometry in PolSAR

It has been more than a decade since the Riemannian manifold embedding is used with PolSAR data, exclusively in evaluating the coherency/covariance matrices.

In the general literature, we have identified different methodologies proposed for this manifold embedding. Some methods operate directly on the Riemannian manifold, while others operate with projections (i.e., onto the tangent space, embeddings of lower dimension, etc.). The proposed method fits the first direction. A short literature review, with techniques and applications that use Riemannian geodesics in PolSAR data manipulation techniques is given below.

In [22, 23], Formont et al. challenge the use of the popular Wishart similarity for measuring the similarity between PolSAR covariance matrices. They modify the Wishart unsupervised classification algorithm of [33] and introduce AIRM as distance metric. Other examples which use the metric for clustering applications are in [47, 60].

In [3, 45], the AIRM distance is used in PolSAR/PolInSAR time-series unsupervised classification with a binary partition tree algorithm applied in the space of covariance matrices. Another method, the nearest regularized subspace, is also modified to incorporate the same manifold metric [46].

The supervised classification of PolSAR data via dictionary learning, the SVM technique and the AIRM metric is employed in [59, 58].

For adaptive PolSAR speckle filtering, [39, 40] propose a modified mean shift algorithm. The method uses a different geodesic distance measure, the

log-Euclidean Riemannian metric and its corresponding gradient, when calculating the local maximum point required by the implementation. This metric is also used for PolSAR supervised classification, e.g., with dictionary learning and the SVM method [56].

Therefore, techniques based on the use of PSD manifold metrics are reported in PolSAR both with preprocessing (i.e., filtering) and data analysis applications performed in the space of  $n \times n, n \in \{3, 4\}$  covariance matrices.

Other manifold metric are introduced, as for example in [44], where Ratha et al. use for the comparison of Kennaugh and covariance matrices the angular geodesic distance, which relies on the assumption of a spherical manifold.

### 1.2.5 Manifold Gradient with Sobel Kernel

For an extended evaluation of Hermitian barycenters, a gradient assessment is performed in the manifold space.

TABLE 1.1: Vertical Sobel kernel. TABLE 1.2: Horizontal Sobel kernel.

-1	0	1
-2	0	2
-1	0	1

-1	-2	-1
0	0	0
1	2	1

The classical Sobel operator [30, 36], known primarily for edge detection in digital image processing, proposes a sample computation of the first order derivative. It operates with two  $3 \times 3$  kernel filters (Tables 1.1, 1.2). Each of them, used as a sliding window, is convoluted with a spatial neighbourhood of the same size to produce the vertical and horizontal gradient components.

We propose an adaptation for gradient computation on the Hermitian manifold. The same weights as in the Sobel kernels multiply barycenter matrices within a  $3 \times 3$  spatial neighbourhood, while an adequate metric is used for distance dissimilarity (AIRM with Hermitian matrices). Both the vertical ( $\mathbf{G}_V$ ) and the horizontal ( $\mathbf{G}_H$ ) manifold gradient components are evaluated.

Considering  $\mathbf{P}^{i,j}$  a barycenter matrix located on row  $i$ , column  $j$ . The following expressions can be written:

$$\mathbf{G}_V^{i,j} = d(\mathbf{P}_\uparrow^{i,j}, \mathbf{P}_\downarrow^{i,j}), \quad (1.11) \quad \mathbf{G}_H^{i,j} = d(\mathbf{P}_{\rightarrow}^{i,j}, \mathbf{P}_{\leftarrow}^{i,j}), \quad (1.12)$$

where

$$\mathbf{P}_\uparrow^{i,j} = \mathbf{P}^{i-1,j-1} + 2\mathbf{P}^{i-1,j} + \mathbf{P}^{i-1,j+1} \quad (1.13)$$

$$\mathbf{P}_\downarrow^{i,j} = \mathbf{P}^{i+1,j-1} + 2\mathbf{P}^{i+1,j} + \mathbf{P}^{i+1,j+1} \quad (1.14)$$

$$\mathbf{P}_{\leftarrow}^{i,j} = \mathbf{P}^{i-1,j-1} + 2\mathbf{P}^{i,j-1} + \mathbf{P}^{i+1,j-1} \quad (1.15)$$

$$\mathbf{P}_{\rightarrow}^{i,j} = \mathbf{P}^{i-1,j+1} + 2\mathbf{P}^{i,j+1} + \mathbf{P}^{i+1,j+1}. \quad (1.16)$$

and the magnitude of the gradient is

$$\mathbf{G} = \sqrt{\mathbf{G}_H^2 + \mathbf{G}_V^2}. \quad (1.17)$$

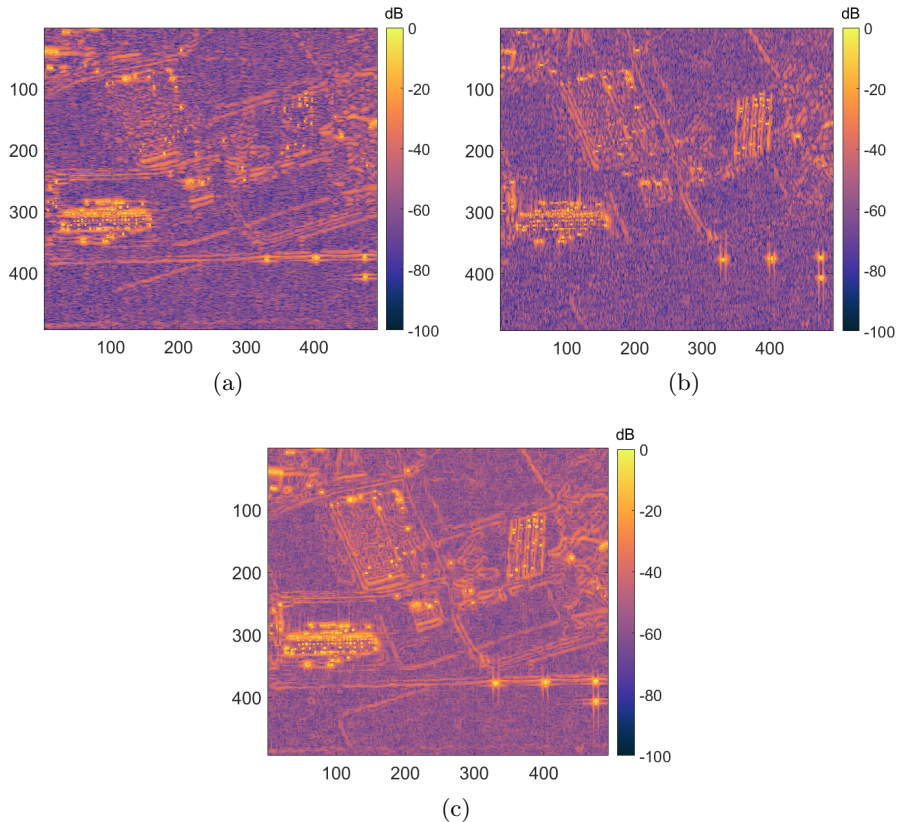


FIGURE 1.2: Brétigny Dataset. Gradient computation for the Hermitian barycenters using the Sobel Filter kernels and the AIRM metric. (a) Horizontal component [dB]. (b) Vertical component [dB]. (c) Magnitude [dB].

Fig. 1.2 shows the Hermitian barycenters Sobel gradient estimate (absolute value, [dB]) for the Brétigny dataset. The shape of the three important structures from the image (horizontal West-Center, left-oblique North-West and right-oblique North-East) is easily distinguished, as well as the field contours. Bright pixels are clearly isolated. A threshold selection may allow for an extraction of coherent scatterers positions similar to that obtained by the 98<sup>th</sup> percentile criterion.

### 1.2.6 Proposed method

The classical k-means algorithm is an iterative, partitioning clustering technique which separates the input data  $X = \{x_i\}, i \in [1, N]$  into  $K$  classes [29, 8]. The method operates by attributing a sample  $x_i$  from the dataset to



class  $K$  through the minimization of a cost function  $\sum_{k=1}^K d(x_i, \mathbf{C}_k)$ , with respect to each cluster centroid  $\mathbf{C}_k$ ,  $k \in [1, K]$ .

We propose a novel algorithm for unsupervised classification which performs k-means clustering on the Riemannian manifold of Hermitian polar factors. Three different processing stages can be identified:

**Step 1:** The scattering matrix is decomposed using the left<sup>1</sup> polar decomposition (1.1), to obtain the Hermitian and unitary factors.

**Step 2:** An identification of coherent scatterers based on the 98<sup>th</sup> percentile criterion proposed by Lee et al. [32] is performed, at first. As in the original algorithm, a  $3 \times 3$  boxcar neighbourhood is used. The pixels fulfilling the criterion are considered to represent coherent targets.

For the coherent scatterers, no additional steps are needed and the Hermitian factors are used directly for clustering (Step 3). With all other pixels, barycenters are otherwise computed. This is the analogous of a N-look geometrical center of mass estimation in the manifold of Hermitian polar factors. The barycenters are computed through an iterative method (1.8) applied in square, local, sliding neighbourhoods of fixed size. The operation of evaluating the Riemannian barycenters in the manifold of Hermitian factors is designated henceforth by acronym *PolBaRi* (*POLar decomposition BARYcenters estimation on the RIemannian manifold*).

**Step 3:** A modified k-means algorithm is applied to the set of points containing barycenters and coherent Hermitian factors. The computation is kept into the native Riemannian manifold of positive-definite matrices using the AIRM metric to evaluate intercluster separation. Here, the class centers are randomly initialized using the k-means++ [4] seeding with the AIRM distance. Progressively, each (barycenter) matrix from the set obtained in Step 2 is allocated to one of the  $K$  classes and the cluster centers are updated. The operation is repeated until the interclass transfer is lower than a predefined threshold (Fig. 1.1).

The suggested algorithm is distinct from other PolSAR Riemannian manifold methods. The state-of-art review in Section 1.2 has evidenced the existence of PolSAR studies using Riemannian distances and/or Riemannian classifiers in the space of covariance/coherency matrices, only. In contrast, we propose to obtain rotation invariant Hermitian factors from the scattering matrix and manipulate such matrices through geometrical averaging and geometric-based clustering techniques.

---

<sup>1</sup>Since similar results have been obtained when considering alternatively the left or right polar decomposition, we refer hereafter exclusively to the use of the left polar factorization.

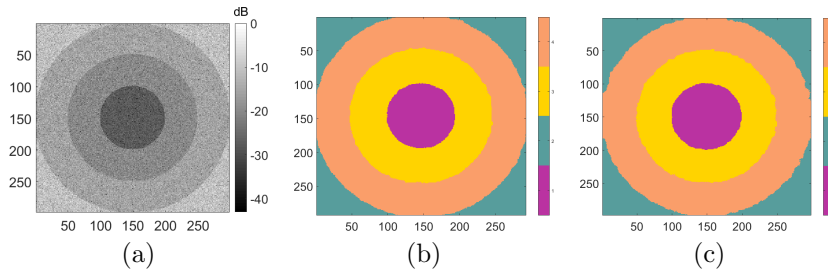


FIGURE 1.3: Simulated data - Dataset 1. (a) 1-look Span [dB]. (b) Wishart Classifier. (c) Proposed method: PolBaRi+Riemannian k-means.

---

### 1.3 Results and discussion

The algorithm introduced in Subsection 1.2.6 is now evaluated on both simulated and real PolSAR data. Each case is addressed in a different subsection. The conventional Wishart classifier, applied on the space of covariance matrices, is used as a benchmark.

In a different subsection we introduce a sample gradient computation technique based on the Sobel kernels, which evaluates the gradient directly on the manifold space.

#### 1.3.1 Simulated datasets

Simulated polarimetric data is obtained through two different methods, as detailed by Subsections 1.3.1.1 and 1.3.1.2.

##### 1.3.1.1 Simulated data with different intensities and covariance matrices

The first simulation technique is a classical method used in the literature [53, 2, 24]. It allows one to create synthetic responses of polarimetric channels with known statistics, i.e., having a known covariance/coherency matrix. In our example, we model four different Gaussian regions, arranged concentrically, as shown in Fig. 1.3a. The intensity is varied linearly from one region to another, with the region bounded by the image border and the second annulus having the highest intensity [2]. The simulated dataset serves as benchmark. The multivariate Gaussian clutter is still the most used statistical model for PolSAR data and represents the best-of-fit distribution for the case of homogeneous regions. With such a statistical model, the Wishart classifier is known to provide the optimum solution [31].

TABLE 1.3: Simulated data - Dataset 1. Per-class accuracy, average class accuracy and kappa coefficients.

Method \ Accuracy	1	2	3	4	Total	
					Acc.	kappa
Wishart classifier	91.45	99.77	99.46	96.7	96.84	0.97
Proposed	99.66	98.81	98.82	98.78	99.02	0.98

Figs.1.3b,c display the results obtained using the Wishart classifier and the proposed method, respectively. For both algorithms, the number of expected classes is provided as input parameter. Table 1.3 contains the percentages of per-class accuracy obtained from the confusion matrices of each classifier. The results are quite similar. With the proposed method, the identification of pixels inside a given class has at least a 98% accuracy, the true-positive percentages being here slightly more homogeneous than with the Wishart classifier. The kappa coefficient is shown in Table 1.3.

### 1.3.1.2 Simulated monostatic backscattering response of a dihedral

With the second simulated dataset, the polarimetric signature of a monostatic right-angle dihedral is modeled. Using an electromagnetic simulation software (here, CST Microwave Studio), the scattered electric field of the elementary target can be obtained from a diverse range of monostatic directions. In the simulations, the object is placed in the center of the coordinate system and rendered from perfect electric conductor material. A spherical coordinate system, described by parameters  $(\theta, \varphi)$  is used. The simulator returns the estimated complex electric field response and, subsequently, which may be then used to estimate the elements of the scattering matrix (linear polarisation).

Fig. 1.4a displays the absolute value of the backscattered electric field, for the right-angle dihedral. The maximum value is obtained at the central point, with coordinates  $(\theta, \varphi) = (0^\circ, 0^\circ)$ . This corresponds to the monostatic canonical dihedral scattering direction in a plane orthogonal to the dihedral's bisector.

In monostatic PolSAR, the response of a dihedral describes the elementary scattering mechanism known as double bounce. Identifying the mechanism from PolSAR data is often indirect, by computing descriptive parameters. One such parameter is the (coherent)  $\alpha_{Cloude}$  value [14]:

$$\alpha_{Cloude} = \cos \left( \frac{1}{\sqrt{2}} \frac{|S_{hh} + S_{vv}|}{|S|_F} \right)^{-1}, \quad (1.18)$$

which is fixed at  $90^\circ$  for the double bounce case.

In Fig. 1.4b the  $\alpha_{Cloude}$  parameter is estimated for each monostatic direction. It is observed that the deviation from the theoretical value remains

acceptable ( $\alpha_{\text{Cloude}} \in [85^\circ, 90^\circ]$ ) when  $\theta, \varphi \in [-45^\circ, 45^\circ]$ . In contrast, for very skewed directions (incidence/scattering predominantly on the exterior edges of the two plates composing the dihedral), the mechanism changes, as expected.

In order to account for noise variation, the data of estimated scattering matrices is not used directly. Instead, at each pixel, multiple Gaussian estimates of the monostatic polarimetric channels are generated by the same method used to obtain the first simulated dataset. After this stage, the PolBaRi estimation is performed pixel-based and the Riemannian k-means is applied. The number of classes is varied between 2-5 (Fig. 1.4c) in order to test the results. Even with the increase in the total number of classes, the technique steadily identifies at the same locations the two main scattering mechanisms shown in Fig. 1.4b. We refer here to the central region of uniform scattering mechanism (in yellow), which corresponds to the double bounce response (as confirmed by the  $\alpha_{\text{Cloude}}$  parameter), and the region from the four exterior corners (second mechanism, i.e., single bounce).

A data profile-cut is extracted along the middle horizontal line in Fig. 1.4b (position marked on left-side with green arrow). This corresponds to backscattering directions presenting right/left variations in azimuth angle, with respect to the evaluation position of the dihedral in the simulations. Considering for this the Hermitian barycenters estimated along the selection line for the k-mean results with two classes (left-side red arrow and dashed line in Fig. 1.4c), two intra-class normalized geometric distances are evaluated.

The upper subfigure of Fig. 1.4d displays the  $\alpha_{\text{Cloude}}$  values. The middle and lower subfigures in Fig. 1.4d contain the normalized AIRM and normalized angular geodesic distances between each of the selected barycenters and the final Hermitian k-means centroid of the corresponding class (i.e., yellow class from Fig. 1.4c).

The angular geodesic between two polar Hermitian factors ( $\mathbf{H}_1, \mathbf{H}_2$ ) preserves the same definition as for Hermitian covariance matrices, [43]:

$$d(\mathbf{H}_1, \mathbf{H}_2) = \frac{2}{\pi} \cos^{-1} \left[ \frac{\text{Tr}(\mathbf{H}_1^H \mathbf{H}_2)}{\sqrt{\text{Tr}(\mathbf{H}_1^H \mathbf{H}_1)} \sqrt{\text{Tr}(\mathbf{H}_2^H \mathbf{H}_2)}} \right]. \quad (1.19)$$

While the  $\alpha_{\text{Cloude}}$  green curve is quite deterministic, both geometric distances (AIRM in red and angular geodesic in magenta) appear random. This is plausibly influenced by the two distinct methods based on which the data was obtained. The  $\alpha_{\text{Cloude}}$  parameter is evaluated directly on the scattering matrices estimated from the electromagnetic simulator. The geometric distances display here similar intra-class separation results.

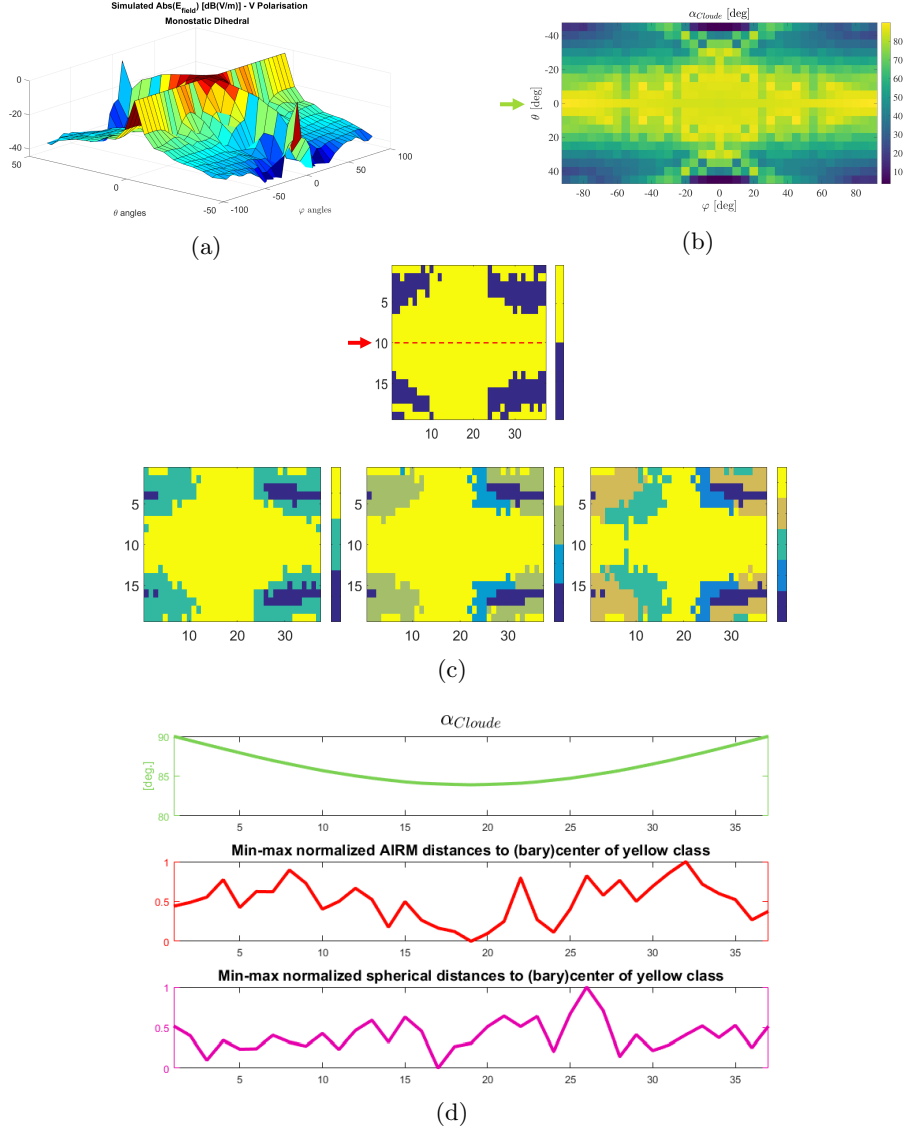


FIGURE 1.4: Simulated data - Dataset 2.  
 (a) Absolute value of the scattered  $E_{field}$ , estimated by the simulation software. (b)  $\alpha_{Clouds}$  angles from estimated scattering matrices. (c) Riemannian k-means clustering result (variable number of classes between 2-5). (d) *Upper:*  $\alpha_{Clouds}$  profile cut variation; *Middle:* Riemannian distance between barycenters along red profile cut in (c) and centroid of the class in yellow. *Lower:* Angular geodesic distance between barycenters along red profile cut in (c) and centroid of the class in yellow.

### 1.3.2 Real datasets

This subsection will illustrate the performance of the proposed clustering algorithm on real monostatic PolSAR data. Foremost, the discussion is extended for the Hermitian and unitary barycenters assessment, now in the context of the real dataset. Afterwards, the results for the clustering method are evaluated.

#### 1.3.2.1 Hermitian barycenters gradient and unitary barycenters parameter estimation

Firstly, we aim to assess for any contextual information present with the unitary barycenters. The points for which the barycenters are not convergent are masked-out and can be observed in white in Figs. 1.5a and 1.5b ( $\approx 25\%$  of the image pixels) .

Starting from a complex unitary matrix,  $\mathbf{U} \in \mathbb{C}^{2 \times 2}$ , with

$$\begin{aligned} \mathbf{U} &= \begin{pmatrix} u_{11} & u_{12} \\ u_{21} & u_{22} \end{pmatrix} \\ &= \begin{pmatrix} |u_{11}| \cdot e^{i\varphi_1} & |u_{12}| \cdot e^{i\varphi_2} \\ |u_{21}| \cdot e^{i\varphi_3} & |u_{22}| \cdot e^{i\varphi_4} \end{pmatrix}. \end{aligned} \quad (1.20)$$

The phase normalized unitary matrix  $\mathbf{U}_{\text{ph-}}$  can be written in parametric form [41]:

$$\begin{aligned} \mathbf{U}_{\text{ph-}} &= \mathbf{U} \begin{pmatrix} e^{-i\varphi_1} & 0 \\ 0 & e^{-i\varphi_4} \end{pmatrix} \\ &= \begin{pmatrix} |u_{11}| & |u_{12}| \cdot e^{i(\varphi_2 - \varphi_4)} \\ |u_{21}| \cdot e^{i(\varphi_3 - \varphi_1)} & |u_{22}| \end{pmatrix} \end{aligned} \quad (1.21)$$

$$= \begin{pmatrix} \cos \theta & -\sin \theta \cdot e^{-i\phi} \\ \sin \theta \cdot e^{i\phi} & \cos \theta \end{pmatrix} \quad (1.22)$$

After performing the phase normalization, as in (1.21), the angular  $\theta$  and phase  $\phi$  parameters are easily obtained for the unitary barycenters of the real dataset. The results are in Fig. 1.5a and Fig. 1.5b, respectively, with histograms below the main figures. It is to be mentioned that with the Brétigny dataset about 25% of the image pixels do not attain unitary barycenter convergence.

The  $\theta$  angle parameter takes values below  $25^\circ$  (Fig. 1.5c), while the phase absolute values are normally spread in the entire  $[0^\circ, 180^\circ]$  interval (Fig. 1.5d). As example, we can observe the zone corresponding to the building located West-Center, where multiple coherent scatterers are present (red ellipse selection). Here, the  $\theta$  values approach zero degrees. The phase values present also an extreme (i.e.  $\pm 180^\circ$ ). Such observations indicate that the phase normalized unitary barycenters at those locations are (almost) identity matrices. In turn, this may also imply that the original unitary polar factors, used in estimating the barycenters, are themselves close to identity. For such a case, the

Hermitian polar factors are completely descriptive and (almost) equal to the original scattering matrices. This result confirms the choice from the design of the PolBaRi algorithm of performing the pre-selection of coherent scatterer and attributing to those locations directly the Hermitian factor, without barycenter estimation.

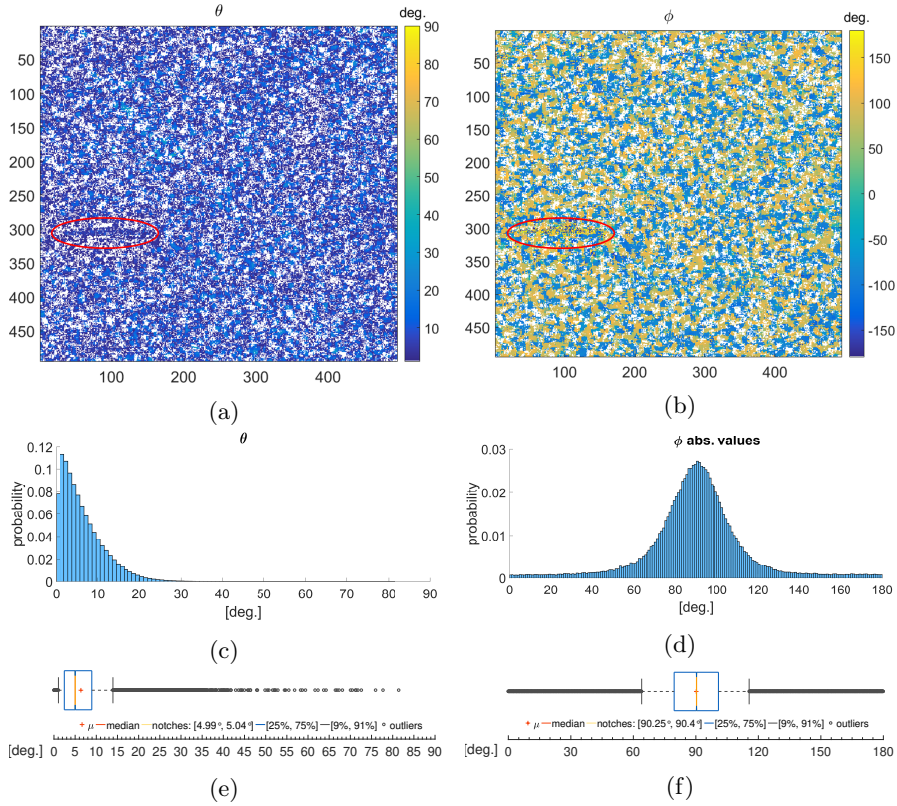


FIGURE 1.5: Brétigny Dataset. (a) Angles obtained from the normalized unitary barycenter matrices [degrees]. (b) Phase values obtained from the normalized unitary barycenter matrices [degrees].

Following statistics are computed excluding white-masked values: (c) Histogram of angles from (a). (d) Histogram of absolute phases from (b). (e) Notches boxplot with mean and median values for angles in (a). (f) Notches boxplot with mean and median values for absolute phase values in (b).

Removing the effect of rotations imposed on the line-of-sight backscattering direction as well as the search of rotation invariant descriptors is of particular interest in polarimetric radar applications. The topic has a significant line of work associated for both coherent and incoherent PolSAR decompositions [13, 48].

In monostatic PolSAR, the term rotation invariant (roll-invariant) is generally used to distinguish a result which does not incorporate the target's rotation angle around the Line of Sight (LOS). Since in the monostatic case this rotation around the LOS has the same effect as an antenna rotation around the same axis, this is equivalent to a rotation of the received signal. Because of this, the target-measurement equivalence rotation compensations are very common. This has been applied in PolSAR with scattering matrices [14], covariance/coherency matrices [34], Kennaugh matrices [44], alike.

Moreover, the rotation invariance is a property used for both targets and descriptive parameters. The computation technique of some parameters may inherently eliminates rotations (e.g., the eigen-decomposition applied to the covariance matrix, which assures that the entropy and average alpha angles are invariant [14]), while for others, the orientation-compensation is applied as prerequisite.

With the proposed polar decomposition, we have shown that the unitary matrices can be described by two random phases and two parametric values (an angle and a phase). With coherent scatterers, discarding the unitary polar factor does not produce significant changes, while for other scatterers the removal of unwanted rotations from the original scattering matrix is highly beneficial. Evidence from both simulated and real data shows that the contextual and spatial information is preserved by the Hermitian polar term. Such observations legitimize the key role of the Hermitian barycenters with the proposed clustering method.

Figs. 1.6a,b compare the results of two different boxcar "averaging" operations. Each image displays the absolute values of the first data channel.

For obtaining Fig. 1.6, the arithmetic mean of scattering matrices (Brétigny dataset) has been computed inside a  $7 \times 7$  (pixels) moving window. Otherwise, Fig. 1.6 contains absolute values (log scale) of the first element of the estimated Hermitian barycenters.

In Fig. 1.6a, the amplitude levels of the different zones are quite similar, which determines that most zones appear mixed up. Coherent scattering points, having a higher amplitude, remain clearly visible. On the contrary, a larger dynamic range is evident for the barycenter image in Fig. 1.6b. Alongside the scatterers of high intensity, the shape and structure of other parts from the original image are clearly distinguishable, for example with vegetation parcels and roads.

The visual inspection proposed between a spatial arithmetic average of scattering matrices and a spatial geometric estimation of a Hermitian centroids shows superior results for the second approach. In light of this comparison, a similarity may be drawn with the results from [26]. The reference compares the difference between arithmetic and geometric averages of single channel multi-temporal SAR series. Improved results in terms of speckle variation and signal to noise ratio are reported for the geometric mean computation, as



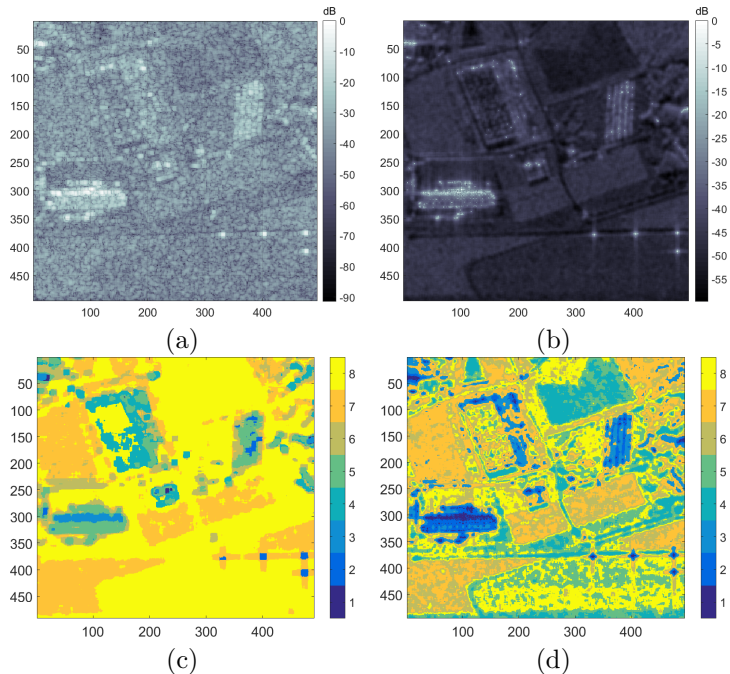


FIGURE 1.6: Brétigny Dataset. (a)  $\mathbf{S}_{11}$  boxcar average (amplitude, [dB]). (b) Hermitian barycenters ( $\mathbf{h}_{11}$ , amplitude, [dB]). (c) Wishart result. (d) PolBaRi+Riemannian k-means result.

long as the SAR images from the acquisitions stack remain similar, with no significant permanent changes.

### 1.3.2.2 Clustering results

In the following, the clustering results obtained by the proposed and the benchmark algorithms are compared. The Riemannian barycenter estimation requires a spatially moving window averaging, while the Wishart implementation performs the boxcar moving averaging to compute the sample coherency matrices. The same size of the moving window,  $7 \times 7$ , is used with both implementations. The first dataset is full-polarimetric, obtained by the French Aerospace Lab RAMSES airborne X-Band radar instrument, over a test site in Brétigny-sur-Orge (France). It is characterized by a resolution of approximate 1.5 m, in both azimuth and range [52].

Figs. 1.6c,d display the classification results for the classical Wishart and the proposed method, respectively. The Wishart estimation operates with 8 classes. The same number has been considered for the PolBaRi+Riemannian k-means implementation. The classes are sorted in an ascending order (blue to yellow).

The global positioning of classes in the two images is similar. One major visual difference concerns the bow-shaped field in the North of Fig. 1.6c, which is assigned to a distinct class. This is the case with other small zones, attributed by the Wishart classification to the 8<sup>th</sup>, yellow class.

Considering, as examples, the horizontal West-Center oriented building and the oblique North-East parking space, the classes identified by the proposed method at the location are in close proximity, while the Wishart classifier brings more distant ones together. However, as the final scattering mechanism interpretation may not be quite the same for the two classifiers and in the absence of a ground truth for the dataset acquisition, there is no categorical validation for the classes.

Without doubt, the most striking difference in the interpretation offered by the two classifiers, is textural. The Wishart result is smooth, largely homogeneous, while the proposed algorithm provides a more heterogeneous result, conserving some of the texture and details of the original image. For example, in the left-side of the parking space (North-East), near the road border, there is an area covered by trees. The Wishart classifier identifies a small group of trees to the south of the parking lot and where some pixels of higher intensity are present, while identification is minimum in the area left to the parking lot. The proposed method better represents the information from the area, even if the pixels are of lower intensity. As second example, one can observe that the roads (contours in Fig. 1.2) blend with the background yellow class in the Wishart classification, whereas they are clearly distinguishable in the PolBaRi+Riemannian k-means result. In the original image they too are represented by pixels of lower intensity.

For completeness, a second real dataset is presented, the well-known PolSAR EMISAR Foulum. This is a C-Band observation over a vegetation-dominated area, with crop fields, forests, a lake and some small urban settlements.

Fig. 1.7a shows the  $h_{1,1}$  data channel from the Hermitian barycenter estimates. The PolBaRi+Riemannian k-means clustering result is presented in Fig. 1.7b and the Wishart k-means clustering is illustrated in Fig. 1.7c. An additional geometric metric has been used for qualitative evaluation, the angular geodesic [43]. The results are displayed in Fig. 1.7d. For comparison purposes, this latter implementation is based on the same k-means framework/initialization, as in the case of Wishart. For display aesthetic, classes are sorted here in descending order (blue to yellow).

With respect to the Wishart classification, the texture information is better preserved when using both geometrical distances. However, the PolBaRi+Riemannian k-means exhibits the best accuracy as it is able to discriminate crop fields which are not retrieved by the other two methods, using the same number of clusters. For example, the L-shaped areas near the image center are correctly separated by the yellow and dark blue classes [17]. In proposed ground-truths of the dataset, the two fields have distinct type of crops, beet and winter wheat. This is in accordance with the results obtained using

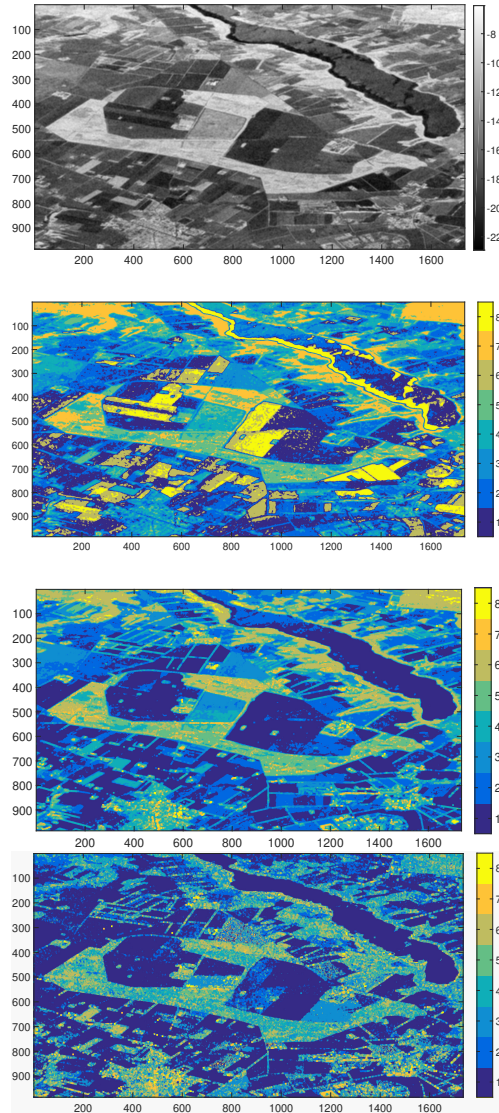


FIGURE 1.7: Foulum Dataset. (a) Hermitian barycenters ( $\mathbf{h}_{1,1}$ , amplitude, [dB]). (b) PolBaRi+Riemannian k-means result. (c) Wishart result. (d) k-means with distance metric the angular geodesic distance.

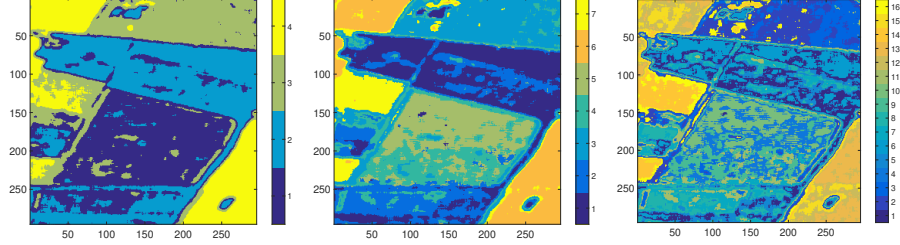


FIGURE 1.8: Foulum Dataset - Region selection. Results of Riemannian k-mean clustering with: (a) 4 classes, (b) 7 classes, (c) 16 classes.

the compound Gaussian mixtures classification model [20], which nonetheless has a higher decrease in spatial resolution.

Given the geometrical nature of the proposed k-means clustering, it is straightforward to define a simple objective criterion for data-driven evaluation of the classification result. By modifying the Calinski-Harabasz (variance ratio) criterion [9] with the AIRM metric, we obtain:

$$\text{CH}_k = \frac{\text{var}_B}{\text{var}_W} \cdot \frac{N - K}{K - 1}, \quad (1.23)$$

$$\text{var}_B = \sum_{i=1}^K n_i \cdot d_{\text{geod}, \mathbb{P}(n)}(\mathbf{C}_i, \mathbf{H}_{\text{tot}})^2, \quad (1.24)$$

$$\text{var}_W = \sum_{i=1}^K \sum_{\mathbf{H}_j \in \mathbf{C}_i} d_{\text{geod}, \mathbb{P}(n)}(\mathbf{H}_j, \mathbf{C}_i)^2, \quad (1.25)$$

where  $N$  is the total number of pixels in the PolSAR image,  $K$  is the number of clusters,  $\mathbf{H}_{\text{tot}}$  is the overall barycenter of the sample PolSAR data and  $n_i$  refers to the number of observations in cluster  $i$ , of centroid  $\mathbf{C}_i$ .

In order to find the correct number of classes, different Riemannian k-mean clustering runs are operated on a  $300 \times 300$  sub-image from the Foulum dataset. Fig. 1.8 shows the results obtained with  $K \in \{4, 7, 16\}$ . For each  $K$ ,  $2 \times K$  trials have been performed and the maximum  $\text{CH}_k$  value has been computed in each case. Fig. 1.9a illustrates the normalized index  $\text{CH}_k$  as function of  $K$ . The optimal number of classes with respect to this sub-dataset corresponds to  $\arg \max_K(\text{CH}_k)$  and equals 7 (Fig. 1.8b). In Fig. 1.9b, the normalized  $\text{CH}_k$  for  $K \in \{8, 16\}$  is computed over the full EMISAR Foulum dataset. In this case, the  $K = 8$  provides a much better match.

In conclusion, different data-driven clustering evaluation strategies can be adopted for the positive definite manifold geometry. One of the benefits of the proposed geometrical clustering is that conventional criteria, such as the Calinski-Harabasz can be used rigorously to optimize the k-means parameters as the AIRM is a true distance.

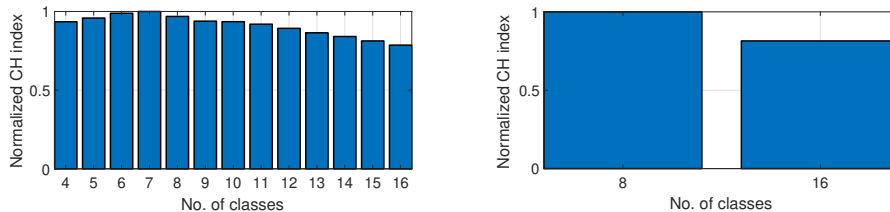


FIGURE 1.9: Foulum Dataset - AIRM Calinski-Harabasz index (normalized display) evaluation. (a) For the data selection in Fig. 1.8. (b) For the entire Foulum image, if  $K = 8$  and  $K = 16$ .

#### 1.4 General Remarks and Conclusions

The proposed method, PolBaRi+Riemannian k-means, is unique in several respects. It incorporates a coherent technique operating on the original scattering matrix (i.e, the polar decomposition) which preserves the matrix format (contrary to the incoherent decomposition methods where data is firstly vectorized). It is to be emphasized that the polar decomposition can be applied to both symmetric and asymmetric scattering matrices and the Hermitian factor is always unique. The data processing resembles also the incoherent techniques, as it proposes a spatial averaging processing on the Riemannian manifold for calculating centroids of Hermitian factors. This allows the applicability of the proposed method even with distributed targets inside a scene. The AIRM Riemannian geodesic metric is used to evaluate matrix dissimilarity both for Hermitian polar factor centroids and in the modified k-means algorithm.

In a distinct contribution of the chapter, the AIRM metric is applied in the development of: a) a sample gradient algorithm based on the Sobel kernels and b) an objective criterion, based on the Calinski-Harabasz variance ratio, for evaluating the number of clusters. Such implementations may prove useful in other applications which involve computations with data embedded in the Riemannian manifold of positive/Hermitian definite matrices.

The proposed clustering algorithm has been compared against two different k-means implementations: the well-known stochastic Wishart and the newer geometric-based angle geodesic clustering. The performance was shown to be competitive with simulated Gaussian clutter data - a case for which the Wishart classifier is known to offer optimum results.

Supplementary experiments are anticipated for better understanding the geometric properties of the two factors from the PolSAR data polar decomposition. As the method can be applied with both symmetric and asymmetric scattering matrices, an envisioned extension is for testing the results with data from quasi-monostatic and bistatic systems. Finally, future work will ad-

dress enhancing the clustering algorithm using Gaussian and non-Gaussian statistics on the manifold of positive definite matrices.

---

## 1.5 Glossary

**AIRM:** Affine Invariant Riemannian Metric

**PolSAR:** Polarimetric Synthetic Aperture Radar

**PSD:** Positive Semi Definite

**SVD:** Singular Value Decomposition

---

## Bibliography

- [1] Charu C. Aggarwal and Chandan K. Reddy, editors. *Data Clustering: Algorithms and Applications*. CRC Press, 2014.
- [2] Alberto Alonso-Gonzalez, Carlos Lopez-Martinez, and Philippe Salmier. Filtering and segmentation of polarimetric SAR data based on binary partition trees. *IEEE Transactions on Geoscience and Remote Sensing*, 50(2):593–605, 2012.
- [3] Alberto Alonso-González, Carlos López-Martínez, and Philippe Salmier. PolSAR time series processing with binary partition trees. *IEEE Transactions on Geoscience and Remote Sensing*, 52(6):3553–3567, 2014.
- [4] David Arthur and Sergei Vassilvitskii. k-means++: The advantages of careful seeding. Technical Report 2006-13, Stanford InfoLab, June 2006.
- [5] Alexandre Barachant, Stéphane Bonnet, Marco Congedo, and Christian Jutten. Multiclass brain–computer interface classification by Riemannian geometry. *IEEE Transactions on Biomedical Engineering*, 59(4):920–928, 2012.
- [6] Rajendra Bhatia. *The Riemannian Mean of Positive Matrices*, pages 35–51. Springer Berlin Heidelberg, Berlin, Heidelberg, 2013.
- [7] Lionel Bombrun, Gabriel Vasile, Michel Gay, and Felix Totir. Hierarchical segmentation of polarimetric SAR images using heterogeneous clutter models. *IEEE Transactions on Geoscience and Remote Sensing*, 49(2):726–737, 2011.
- [8] Surekha Borra, Rohit Thanki, and Nilanjan Dey. *Satellite Image Analysis: Clustering and Classification*. Springer Nature, Singapore, 2019.
- [9] T. Caliński and J Harabasz. A dendrite method for cluster analysis. *Communications in Statistics*, 3(1):1–27, 1974.
- [10] Fang Cao, Wen Hong, Yirong Wu, and Eric Pottier. An unsupervised segmentation with an adaptive number of clusters using the  $span/h/\alpha/a$  space and the complex wishart clustering for fully polarimetric sar data analysis. *IEEE Transactions on Geoscience and Remote Sensing*, 45(11):3454–3467, 2007.

- [11] L. Carrea and G. Wanielik. Polarimetric SAR processing using the polar decomposition of the scattering matrix. In *IGARSS 2001. Scanning the Present and Resolving the Future. Proceedings. IEEE 2001 International Geoscience and Remote Sensing Symposium*, volume 1, pages 363–365 vol.1, 2001.
- [12] L. Carrea, G. Wanielik, and L. Giubolini. The polar decomposition of the scattering matrix applied to the polarimetric image of the guard-rail. In *14th International Conference on Microwaves, Radar and Wireless Communications. MIKON - 2002. Conference Proceedings*, volume 2, pages 563–566 vol.2, 2002.
- [13] Jiehong Chen, Hong Zhang, Chao Wang, and Junsong Jia. Roll-invariant target parameter extraction from POLSAR data. *IEEE Journal of Selected Topics in Applied Earth Observations and Remote Sensing*, 12(11):4502–4516, 2019.
- [14] Shane Cloude. *Polarisation: Applications in Remote Sensing*. Oxford University Press, Oxford, 2009.
- [15] S.R. Cloude and E. Pottier. An entropy based classification scheme for land applications of polarimetric SAR. *IEEE Transactions on Geoscience and Remote Sensing*, 35(1):68–78, 1997.
- [16] Marco Congedo, Bijan Afsari, Alexandre Barachant, and Maher Moakher. Approximate joint diagonalization and geometric mean of symmetric positive definite matrices. *PLOS ONE*, 10(4):1–25, 04 2015.
- [17] Hongwei Dong, Lamei Zhang, and Bin Zou. PolSAR image classification with lightweight 3D convolutional networks. *Remote Sensing*, 12(3), 2020.
- [18] Anthony P. Doulgeris, Stian Normann Anfinsen, and Torbjørn Eltoft. Classification with a non-Gaussian model for PolSAR data. *IEEE Transactions on Geoscience and Remote Sensing*, 46(10):2999–3009, 2008.
- [19] Anthony P. Doulgeris, Stian Normann Anfinsen, and Torbjørn Eltoft. Automated non-Gaussian clustering of polarimetric synthetic aperture radar images. *IEEE Transactions on Geoscience and Remote Sensing*, 49(10):3665–3676, 2011.
- [20] A.P. Doulgeris and T. Eltoft. Scale mixture of gaussian modelling of polarimetric SAR data. *EURASIP Journal on Advances in Signal Processing*, 1:1687–6180, 2010.
- [21] Simone Fiori and Toshihisa Tanaka. An algorithm to compute averages on matrix Lie groups. *IEEE Transactions on Signal Processing*, 57(12):4734–4743, 2009.



- [22] P. Formont, J.P. Ovarlez, F. Pascal, G. Vasile, and L. Ferro-Famil. On the extension of the product model in POLSAR processing for unsupervised classification using information geometry of covariance matrices. In *2011 IEEE International Geoscience and Remote Sensing Symposium*, pages 1361–1364, 2011.
- [23] Pierre Formont, Jean-Philippe Ovarlez, and Pascal Frédéric. *On the Use of Matrix Information Geometry for Polarimetric SAR Image Classification*. Springer Berlin Heidelberg, Berlin, Heidelberg, 2013.
- [24] Samuel Foucher and Carlos López-Martínez. Analysis, evaluation, and comparison of polarimetric SAR speckle filtering techniques. *IEEE Transactions on Image Processing*, 23(4):1751–1764, 2014.
- [25] A.C. Frery, Abraão D. C. Nascimento, and Renato J. Cintra. Analytic expressions for stochastic distances between relaxed complex Wishart distributions. *IEEE Transactions on Geoscience and Remote Sensing*, 52(2):1213–1226, 2014.
- [26] Nicolas Gasnier, Loïc Denis, and Florence Tupin. On the use and denoising of the temporal geometric mean for SAR time series. *IEEE Geoscience and Remote Sensing Letters*, 19:1–5, 2022.
- [27] Luis Gomez, Jie Wu, and A.C. Frery. Nonlocal means filters for full polarimetric synthetic aperture radar images with stochastic distances. *Image Processing On Line*, 12:142–172, 2022.
- [28] G.C. Hu and Q.H. Zhao. G0-Wishart distribution based classification from polarimetric SAR images. *ISPRS Annals of the Photogrammetry, Remote Sensing and Spatial Information Sciences*, IV-2/W4:451–455, 2017.
- [29] Anil K. Jain. Data clustering: 50 years beyond k-means. *Pattern Recognition Letters*, 31(8):651–666, 2010. Award winning papers from the 19th International Conference on Pattern Recognition (ICPR).
- [30] Chung Chang Lee. Elimination of redundant operations for a fast Sobel operator. *IEEE Transactions on Systems, Man, and Cybernetics*, SMC-13(2):242–245, 1983.
- [31] J.-S. Lee, M.R. Grunes, and R. Kwok. Classification of multi-look polarimetric SAR imagery based on complex Wishart distribution. *International Journal of Remote Sensing*, 15(11):2299–2311, 1994.
- [32] Jong-Sen Lee, Thomas L. Ainsworth, Yanting Wang, and Kun-Shan Chen. Polarimetric SAR speckle filtering and the extended Sigma filter. *IEEE Transactions on Geoscience and Remote Sensing*, 53(3):1150–1160, 2015.

- [33] Jong-Sen Lee, M.R. Grunes, T.L. Ainsworth, Li-Jen Du, D.L. Schuler, and S.R. Cloude. Unsupervised classification using polarimetric decomposition and the complex Wishart classifier. *IEEE Transactions on Geoscience and Remote Sensing*, 37(5):2249–2258, 1999.
- [34] Jong-Sen Lee, M.R. Grunes, E. Pottier, and L. Ferro-Famil. Unsupervised terrain classification preserving polarimetric scattering characteristics. *IEEE Transactions on Geoscience and Remote Sensing*, 42(4):722–731, 2004.
- [35] Shih-Yau Lu and Russell A. Chipman. Interpretation of Mueller matrices based on polar decomposition. *J. Opt. Soc. Am. A*, 13(5):1106–1113, May 1996.
- [36] Paul Mather and Magaly Koch. *Computer Processing of Remotely-Sensed Images: An Introduction, Fourth Edition*. John Wiley and Sons Ltd, UK, 2011.
- [37] Maher Moakher. A differential geometric approach to the geometric mean of symmetric positive-definite matrices. *SIAM Journal on Matrix Analysis and Applications*, 26(3):735–747, 2005.
- [38] Patrizio Neff, Yuji Nakatsukasa, and Andreas Fischle. A logarithmic minimization property of the unitary polar factor in the spectral and Frobenius norms. *SIAM Journal on Matrix Analysis and Applications*, 35(3):1132–1154, 2014.
- [39] Bo Pang, Shi-qi Xing, Yong-zhen Li, and Xue-song Wang. Speckle filtering algorithm for polarimetric SAR based on mean shift. In *2012 IEEE International Geoscience and Remote Sensing Symposium*, pages 5892–5895, 2012.
- [40] Bo Pang, Shiqi Xing, Yongzhen Li, and Xuesong Wang. Novel polarimetric SAR speckle filtering algorithm based on mean shift. *Journal of Systems Engineering and Electronics*, 24(2):222–223, 2013.
- [41] John Polcari. Butterfly decomposition of arbitrary unitary matrices. Working paper, 2014.
- [42] Xianxiang Qin, Yanning Zhang, Ying Li, Yinglei Cheng, Wangsheng Yu, Peng Wang, and Huanxin Zou. Distance measures of polarimetric SAR image data: A survey. *Remote Sensing*, 14(22), 2022.
- [43] Debanshu Ratha, Avik Bhattacharya, and A.C. Frery. Unsupervised classification of PolSAR data using a scattering similarity measure derived from a geodesic distance. *IEEE Geoscience and Remote Sensing Letters*, 15(1):151–155, 2018.

- [44] Debanshu Ratha, Eric Pottier, Avik Bhattacharya, and A.C. Frery. A PolSAR scattering power factorization framework and novel roll-invariant parameter-based unsupervised classification scheme using a geodesic distance. *IEEE Transactions on Geoscience and Remote Sensing*, 58(5):3509–3525, 2020.
- [45] Philippe Salembier and Samuel Foucher. Optimum graph cuts for pruning binary partition trees of polarimetric SAR images. *IEEE Transactions on Geoscience and Remote Sensing*, 54(9):5493–5502, 2016.
- [46] Junfei Shi and Haiyan Jin. Riemannian nearest-regularized subspace classification for polarimetric SAR images. *IEEE Geoscience and Remote Sensing Letters*, 19:1–5, 2022.
- [47] Hui Song, Wen Yang, Neng Zhong, and Xin Xu. Unsupervised classification of PolSAR imagery via kernel sparse subspace clustering. *IEEE Geoscience and Remote Sensing Letters*, 13(10):1487–1491, 2016.
- [48] Boularbah Souissi and Mounira Ouarzeddine. Analysis of orientation angle shifts on the polarimetric data using Radarsat2 images. *IEEE Journal of Selected Topics in Applied Earth Observations and Remote Sensing*, 9(4):1331–1342, 2016.
- [49] Jean-Claude Souyris and Celine Tison. Polar decomposition and polarimetric SAR analysis: A quaternion approach. In *2006 IEEE International Symposium on Geoscience and Remote Sensing*, pages 1752–1755, 2006.
- [50] Jean-Claude Souyris and Celine Tison. Multi-look polar decomposition of polarimetric SAR images. In *2007 IEEE International Geoscience and Remote Sensing Symposium*, pages 4144–4147, 2007.
- [51] Jean-Claude Souyris and Celine Tison. Polarimetric analysis of bistatic SAR images from polar decomposition: A quaternion approach. *IEEE Transactions on Geoscience and Remote Sensing*, 45(9):2701–2714, 2007.
- [52] Laetitia Thirion-Lefevre and Régis Guinvarch. The double Brewster angle effect. *Comptes Rendus Physique*, 19(1):43–53, 2018.
- [53] Gabriel Vasile, Jean-Philippe Ovarlez, Frederic Pascal, and Céline Tison. Coherency matrix estimation of heterogeneous clutter in high-resolution polarimetric SAR images. *IEEE Transactions on Geoscience and Remote Sensing*, 48(4):1809–1826, 2010.
- [54] Hanning Wang, Zhimin Zhou, John Turnbull, Qian Song, and Feng Qi. PolSAR classification based on generalized polar decomposition of Mueller matrix. *IEEE Geoscience and Remote Sensing Letters*, 13(4):565–569, 2016.

- [55] Wen Yang, Hui Song, Gui-Song Xia, and Carlos López-Martínez. Dissimilarity measurements for processing and analyzing PolSAR data: A survey. In *2015 IEEE International Geoscience and Remote Sensing Symposium (IGARSS)*, pages 1562–1565, 2015.
- [56] Xiangli Yang, Wen Yang, Hui Song, and Pingping Huang. Polarimetric SAR image classification using geodesic distances and composite kernels. *IEEE Journal of Selected Topics in Applied Earth Observations and Remote Sensing*, 11(5):1606–1614, 2018.
- [57] S.H. Yueh, J.A. Kong, J.K. Jao, R.T. Shin, and L.M. Novak. K-Distribution and polarimetric terrain radar clutter. *Journal of Electromagnetic Waves and Applications*, 3(8):747–768, 1989.
- [58] Yachao Zhang, Xuan Lai, Yuan Xie, Yanyun Qu, and Cuihua Li. Geometry-aware discriminative dictionary learning for PolSAR image classification. *Remote Sensing*, 13(6), 2021.
- [59] Neng Zhong, Tianheng Yan, Wen Yang, and Gui-Song Xia. A supervised classification approach for PolSAR images based on covariance matrix sparse coding. In *2016 IEEE 13th International Conference on Signal Processing (ICSP)*, pages 213–216, 2016.
- [60] Neng Zhong, Wen Yang, Anoop Cherian, Xiangli Yang, Gui-Song Xia, and Mingsheng Liao. Unsupervised classification of polarimetric SAR images via Riemannian sparse coding. *IEEE Transactions on Geoscience and Remote Sensing*, 55(9):5381–5390, 2017.